A novel pipeflow manipulation technique for subsurface thermal applications

Nawaf Salem[a], Ali Tarokh[b], Arman Hemmati[a,*]

[a]*Department of Mechanical Engineering, University of Alberta, Edmonton, Canada*
[b]*Department of Mechanical Engineering, Lakehead University, Thunder Bay, Canada*

Abstract

This numerical study evaluates the performance of a new pipe-insert technology that reduces heat losses to the ground formation in subsurface thermal systems, such as geothermal energy harvesting. Particularly, we examine the capacity of three targeted pipe inserts on reducing heat convection and frictional drag of turbulent pipeflow at Reynolds number of 7.5×10^4. The newly introduced pipe-inserts incorporate 3-dimensional wall shape variations that resemble targeted azimuthal Fourier modes in wall-bounded turbulence. These pipe-inserts output flow features that render extensive economic and ecological benefits pertinent to extraction and transportation of thermal energy. Targeted pipe shapes generate extended downstream region of suppressed heat convection and reduced frictional drag by means of turbulent pipeflow manipulation. The results indicate that imposing targeted shapes for the pipe cause flow deceleration and reduced velocity gradients in near-wall region, leading to concurrent reductions in convective heat transfer and frictional drag. Particularly, the results exhibit a maximum reduction of ∼9% in near-wall heat transfer for two wall shapes, compared to a smooth pipe. The fully-developed thermal condition is recovered at an axial location of $x/D = 40$ from the perturbation, where D is the pipe diameter. Further, a significant attenuation in skin-frictional drag is observed, hinting at maximum decrease of 17.4% and 16.5% for two pipe-insert shapes. At $x = 2D - 10D$ following the inserts, the averaged reductions in near-wall convective heat transfer and frictional drag for one of the targeted inserts correspond to 3.4% and 5.0%, respectively.

Keywords: Turbulent pipe flow, Heat transfer, RANS, Wall shape modifications, Geothermal systems

*Corresponding author.
Email address: arman.hemmati@ualberta.ca (A. Hemmati).

1. Introduction

The growing world population and global economy procure to a substantial rise in global energy demand [1]. Currently, this demand is primarily satisfied by non-renewable energy resources, i.e., 78.3% fossil fuels and 2.5% neclear, while the contribution of renewable energies is approximately 19.2% [2]. The utilization of fossil fuels leads to significant greenhouse gas emissions (GHG), which is a leading cause of climate change [1, 3]. For example, heating processes of natural gas in oil-sand industry accounts for 11% of Canada's national GHG emissions [4]. Further, consumption of hydrocarbons contributes to air and water pollution, consequently harming human health, damaging aquatic ecosystems, and threatening the existence of wildlife [5, 6]. These escalating concerns on the detrimental impacts of fossil fuels have sparked a global initiative for energy transition towards sustainable renewable energy systems at competitive costs [7].

Geothermal reserves are of great interest for sustainable renewable energy harvesting. According to the assessment of WEC [8], the overall obtainable geothermal energy is 1.5×10^{21} kWh. It should be noted that the current global energy demand is 7.5×10^{14} kWh, which can be sustained for 2000 years by exploiting only 0.1% of the available geothermal energy [9]. Geothermal energy systems can be employed for electricity production and/or direct use, depending on the extracted energy [10]. Convectional geothermal resources, known as hydrothermal systems, are geologically limited to locations that exhibit high thermal gradients and substantial amounts of hot groundwater [11]. These constraints have led to the evolution of enhanced geothermal systems (EGS), which are characterized as geographically-abundant geothermal reserves. EGS utilizes fracturing to extract commercial-scale thermal energy from low-permeability and/or low-porosity geothermal reserves [12]. A typical EGS is constrcuted by installing one or multiple wells into the impermeable geothermal reservoir and injecting pressurized water to create fractures (enhancing reservoir permeability) [11, 13]. The injected fluid gradually absorbs heat from subsurface highly-heated dry rocks. The heated fluid is sequentially extracted to surface through a production well.

Geothermal systems have the largest capacity factor among various conventional and alternative sources of energy. However, development of global-scale geothermal energy harvesting systems faces many technological challenges. A major challenge is the existence of significant heat losses to the ground rock formations in the extraction processes through production wells [14, 11]. Heat losses to ground rock formations substantially affect the efficiency of geothermal systems and impedes their development as a major alternative source of energy. It is essential to recognize that heat losses to ground formations appear to evolve in various thermal systems, including recovery processes of thermal energy from depleted oil sands reservoirs. Particularly, examinations of steam-assisted gravity drainage (SAGD) operations revealed that approxi-

mately 2/3 of the injected thermal energy is stored by the reservoir, which hints at the feasibility of recovering this thermal energy after the SAGD process is completed [15]. Recovery of this thermal energy can be targeted to offset GHG emissions associated with SAGD processes as well as to generate power efficiently. However, this process is significantly impacted by the existing deficiency related to heat losses.

The challenges outlined thus far hint at the need for (1) attenuating near-wall convective heat transfer that impedes heat losses to ground formations in subsurface thermal systems and (2) lowering skin-friction drag, which results in reduced pumping power requirement. These multiple operational benefits will enhance the capacity of subsurface thermal systems, e.g., geothermal applications and energy recovery operations from depleted oil sands reservoirs. Hence, this contributes to significant reductions in GHG emissions from fossil fuels.

Limited studies exist in literature regarding the attenuation of convective heat transfer in turbulent flows, despite their practical significance for enhancing the efficiency of subsurface thermal systems. Contrarily, flow manipulation techniques that aim to enhance convective heat transfer in wall-bounded flows have been the focus of many studies within the thermal sciences and engineering community. Heat transfer intensification methods are broadly categorized into three classes, i.e., active, passive, and compound [16]. Passive methods employ modifications in surface geometry, which include deployment of artificial roughness elements [17], change in cross-sectional shape [18, 19], and presence of wall curvature in the form of corrugated and wavy surfaces [20, 21]. The modifications in wall shape are essentially aimed to promote effective transverse entrainment between wall and core flow regions and introduce local turbulence [22]. These flow manipulations lead to effective disturbance of thermal boundary layer, resulting in enhanced heat transfer. However, an increase in frictional drag is the unavoidable drawback of deploying such augmentation technique, causing an increase in pumping power requirement [23].

Artificial roughness elements have significant impacts on local and overall convective heat transfer coefficients. In the study of turbulent flow past transverse ribs attached on a duct surface [24], Nusselt number was doubled in comparison to smooth wall condition, while an increment of 4.25 was obtained for friction factor ratio. Lu and Jiang [17] sketched the effects of inclined roughness elements on heat transfer characteristics and friction factor. The orientation of the roughness element with respect to the flow direction was varied between 0° to 90°. At angles of 20° and 60°, the overall thermo-hydraulic performance was superior. Promvonge and Thiangpong [25] studied the effects of ribs in various shapes (rectangular, triangular, and wedge) installed in different arrangements (staggered or in-line) on flow and heat transfer characteristics of fully-developed turbulent flow at $Re = 4 \times 10^3 - 16 \times 10^3$. For similar operating conditions, inline configuration of wedged elements presented higher heat transfer coefficient and friction factor. Further, a three-dimensional numerical study

examined heat transfer implications of four different roughness elements with targeted cross-sectional shapes (circular, square, trapezoidal, and saw-tooth) [26]. The deployment of saw-tooth rib resulted in higher convective heat transfer coefficients.

Modifications to the pipe cross-section have considerable impacts on inducing vortical motions, resulting in better mixing and augmented heat transfer [27, 28]. Patankar et al. [29] performed the first numerical investigation on the characteristics of flow and convective heat transfer in ducts with cyclic-axial alterations in cross-sectional shape. The authors generalized the concept of fully-developed flow condition to accommodate these geometrical variations. Guo et al. [30] suggested that heat transfer process can be intensified by increasing the included angle between temperature gradient and velocity vectors. This ensured that flow entrainment is directed towards the wall boundary, thus increasing radial thermal gradients, which result in higher convective heat transfer coefficients. Following this principle, which is now referred to as field synergy principle, a novel pipe configuration, named as alternating elliptical axis (AEA) tube, was proposed by Meng [31]. The AEA tube was constructed from elliptical tube segments with varying axes, which were bridged using transition joints. The thermal-hydraulic performance of AEA pipe configuration was investigated experimentally by Meng et al. [27] and numerically by Li et al. [28]. They concluded that changes in the cross-sectional geometry in AEA tube induced multi-longitudinal vortical flow motions, which contributed to a substantial intensification in convective heat transfer. Khaboshan and Nazif [32] simulated turbulent forced-convection flow to study the impacts of alternating angle, defined as the angle between the major axis of elliptical cross-sectional planes of the AEA tube, on heat transfer characteristics. The results revealed that increasing the alternating angle led to the increase in the number of longitudinal vortices from four to eight. Inducing more vortical motions in the tube resulted in better entrainment of the core flow towards the near-wall region, which eventually led to augmented heat transfer.

Given the superior performance of wavy surfaces in intensifying convective heat transfer, wavy-walled passages have been commonly implemented in several thermal applications, where geometrical constraints are stringent [33]. Turbulent flow past wavy-walled passage was first investigated by Goldstein Jr and Sparrow [34]. Their results indicated a three-times increase in convective heat transfer coefficient compared to smooth channel flow for low Reynolds number turbulent flows ($Re = 6.0 \times 10^3 - 8.0 \times 10^3$). Later on, it was discovered that wavy-walled passages contributed to a significant enhancement of convective heat transfer only when the flow was in the transitional-flow regime, at which self-sustained oscillatory flow structures were detected [35, 36]. This was attributed to the self-persisted oscillatory flow motions, which destabilized thermal boundary layer and enhanced entrainment between near-wall and core flow regions. This consequently provided a mechanism for heat transfer enhancement. Large eddy simulations (LES) were conducted by Choi and

Suzuki [37] to study heat transfer characteristics of turbulent flow over a channel with one wavy surface. It was elaborated that the surface modification caused the separation of the turbulent shear layer and the formation of near-wall streamwise vortical structures. The imprints of these flow features on the augmentation of the convective heat transfer coefficient were emphasized. Further, Kruse et al. [38] and Kruse and Von Rohr [39] experimentally studied turbulent heat flux of water channel flow with a wavy heated surface. Through detailed inspections, it was revealed that large scale flow motions had the profound effects on the streamwise component of turbulent heat flux while the wall-normal heat flux was mainly dominated by small scale flow structures. Following that, Kuhn et al. [40] simulated three-dimensional turbulent flow over a wavy heated wall and studied the imprints of coherent flow structures on the distribution of the connective heat transfer coefficient. The spatial reorganization of coherent flow structures caused a substantial increase in the overall heat transfer coefficient, up to 2.5 compared to the flat channel configuration.

As discussed previously, there exists a knowledge gap in literature regarding the mitigation of convective heat transfer through deployment of wall-shape modifications. The current study aims to introduce a new mechanism for transporting heated fluid through the subsurface casing that reduces heat losses and frictional drag. More recently, in response to pipe-wall modifications based on distinct Fourier modes, the experiments of Van Buren et al. [41] and the simulations of Masoumifar et al. [42, 43] presented significant capabilities of these wall-shape variations in manipulating pipeflow dynamics. Particularly, they discovered that these wall-shape modifications caused a deceleration of mean flow and reduced velocity gradients in near-wall region, downstream of pipe-insert section. These features can be utilized to manipulate the flow in transport of fluid and energy products towards lowering frictional drag and heat losses. These favorable implications will improve the capacity and efficiency of geothermal systems and energy recovery processes from depleted oil sands reservoirs. Hence, the current study establishes on the experimental [41] and numerical [42, 43] studies to evaluate the capacity of targeted pipe-wall modifications in reducing near-wall convective heat transfer and frictional drag of turbulent pipeflow at $Re = 7.5 \times 10^4$. The pipe-wall changes resembles certain azimuthal Fourier modes of $m = 3$, $m = 15$, and $m \in 3 + 15$. The outcomes presented in this work could be translated to lower our global reliance on hydrocarbons, while reducing greenhouse gas emissions associated with their extraction.

The present study is organized such that the description of the problem and the employed numerical model are illustrated in Section 2. This is followed by the verification and validation of the numerical results in Section 3. Illustration of the results and their discussion are presented in Section 4. The main conclusions of the current study are summarized in Section 5.

2. Problem description

This study is motivated by industrial needs for a new technology that lowers heat losses in casings of subsurface thermal systems. Particularly, this study aims to facilitate extraction and harvesting of energy using subsurface thermal resources (e.g., naturally-geothermal and/or depleted oil sands reservoirs) through introducing a new casing pipe system. Significant heat dissipation to ground formations was reported as a major obstacle during the extraction of heated fluids from subsurface thermal reserves [11, 14]. Hence, we aim to restrain near-wall heat convection and frictional drag of turbulent pipe flow by implementing a novel flow manipulation strategy. These hydrodynamic and thermal features will enhance the capacity of subsurface thermal systems. These features are imposed through targeted wall-shape pipe inserts positioned intermittently in casings or subsurface tubings.

The present study aims at quantitatively evaluating thermal response and recovery of turbulent pipe flow impeded by targeted wall perturbations at $Re = 7.5 \times 10^4$, through comparisons against fully-developed smooth-pipe conditions. These comparisons provide detailed characterization on impacts of distinct pipe-inserts on suppressing near-wall heat convection. Similarly, implications of targeted wall shapes on skin-frictional drag are investigated. Geometrical shapes of the targeted perturbations were designed to closely replicate three azimuthal Fourier modes of $m = 3$ (Case I), $m = 15$ (Case II), and $m = 3{+}15$ (Case III). Schematic illustrations of the targeted perturbations are shown in Figs 1, 2, and 3. The perturbation amplitude (a_m) translated evenly along the streamwise (axial) direction, following a sinusoidal function. The wall corrugation was mathematically formulated as:

$$r\left(\theta, m, x\right) = \frac{D}{2}\left[1 + \frac{\cos(\frac{\pi x}{2D}) + 1}{2}\sum_{m} a_m \sin\left(m\theta\right)\right]. \tag{1}$$

Here, r represents the radial distance, $\theta \in [0, 2\pi]$ denotes the azimuthal angle, and $x \in [-2D, 2D]$ symbolizes the axial (streamwise) location. The perturbation amplitude was $a_{m_1} = 0.2$ for Case I, $a_{m_2} = 0.1$ for Case II, and $a_{m_3} \in \{0.2, 0.1\}$ for Case III. The maximum height (h) of the targeted geometries was $0.1D$ for Case I, $0.05D$ for Case II, and $0.15D$ for Case III. The change in perturbations cross-sectional area can be fully described as $\Delta A = \frac{1}{2}\sum_m (2a_m/D)^2$, with the maximum modulation of 2% for Case I, 0.5% for Case II, and 2.5% for Case III [41].

2.1. Numerical setup

The numerical model involved solving the incompressible Continuity, Reynolds-averaged Navier-Stokes (RANS), and energy equations using OpenFOAM. The numerical simulations were performed at bulk Reynolds number of 7.5×10^4, based on

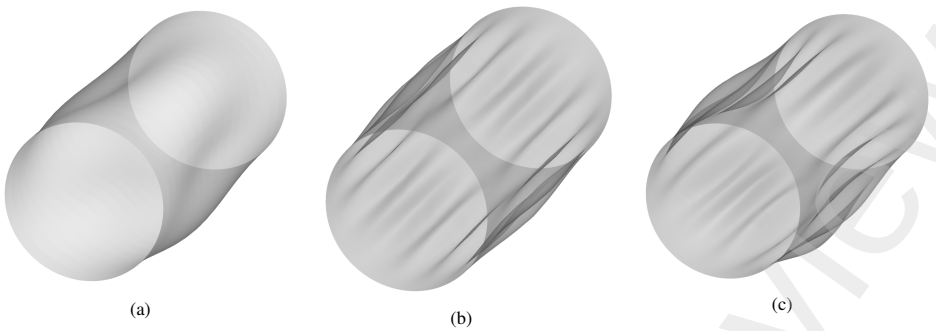

Figure 1: Scematics illustrations of targeted pipe-inserts, (a) $m = 3$, (b) $m = 15$, and (c) $m = 3 + 15$.

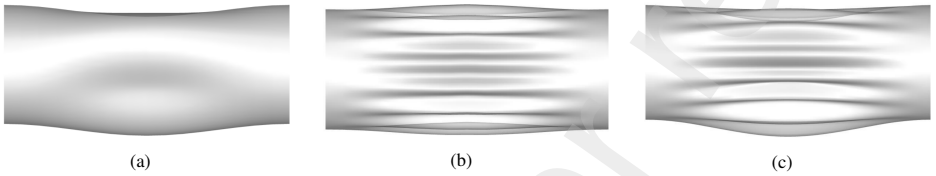

Figure 2: Side-view representation of targeted pipe-inserts, (a) $m = 3$, (b) $m = 15$, and (c) $m = 3 + 15$..

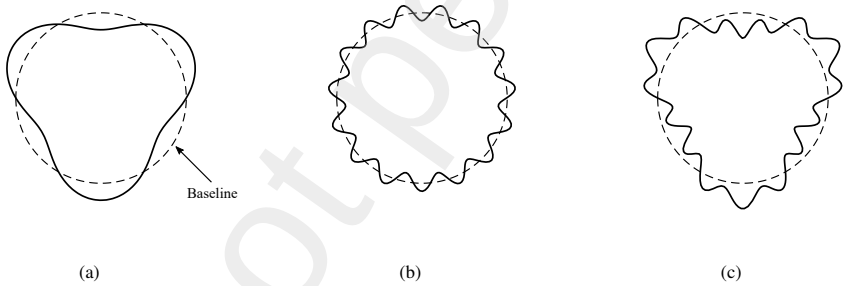

Figure 3: Schematics of the pipe-insert cross-sectional shapes at $x/D = 0$: (a) $m = 3$ (Case I), (b) $m = 15$ (Case II), (c) $m = 3 + 15$ (Case III).

$Re = U_\infty D/\nu$, where U_∞ is averaged inlet velocity of the smooth pipe with a diameter D, and ν is molecular kinematic viscosity of working fluid. Thermophysical properties of the fluid were assumed constant and independent from temperature changes. Table 1 presents the fluid thermophysical properties based on film temperature. The current study assumed negligible effects of radiation and natural convection heat transfer,

Table 1: Thermophysical properties of water at film temperature (T_f).

Parameter	Unit	Value
Density (ρ)	kg/m^3	997
Kinematic viscosity (ν)	m^2/s	8.93×10^{-7}
Thermal conductivity (k_f)	W/m.K	0.61
Specific heat capacity (C_p)	J/kg.K	4181

body forces, and viscous dissipation. Further, steady-state condition was considered. Through implementing the aforementioned assumptions, the governing equations were mathematically formulated as [44],

$$\frac{\partial \overline{U_i}}{\partial x_i} = 0, \tag{2}$$

$$\rho\left(\overline{U_j}\frac{\partial \overline{U_i}}{\partial x_j}\right) = \frac{\partial}{\partial x_j}\left[-\overline{p}\delta_{ij} + \mu\left(\frac{\partial \overline{U_i}}{\partial x_j} + \frac{\partial \overline{U_j}}{\partial x_i}\right) - \rho\overline{u_i' u_j'}\right], \tag{3}$$

$$\rho c_p\left(\overline{U_i}\frac{\partial \overline{T}}{\partial x_i}\right) = \frac{\partial}{\partial x_i}\left(\alpha\frac{\partial \overline{T}}{\partial x_i} - \overline{u_i' T'}\right). \tag{4}$$

where u, p, and T denote the flow velocity, pressure, and temperature, respectively. Turbulent Prandtl number (Pr_t) was set to 0.85, following previous studied in literature of similar perturbed flows [32, 45]. The $k-\omega$ Shear Stress Transport (SST) model was selected for modeling turbulence in the current study based on its adequacy to accurately predict mean flow and heat transfer features of turbulent flows disturbed by geometric wall variations [46, 47, 48, 49, 50, 51, 52]. Further details on mathematical formulations of the $k-\omega$ SST turbulence model can be found in Menter's study [46]. We performed extensive validation studies to assess the accuracy of the $k-\omega$ SST model in predicting the main flow and heat transfer characteristics, the details of which are presented in Section 3.

A computational domain, extending from $-27D$ to $+92D$ in the streamwise direction ($x-$ direction), was employed in the present study. The adequacy of the com-

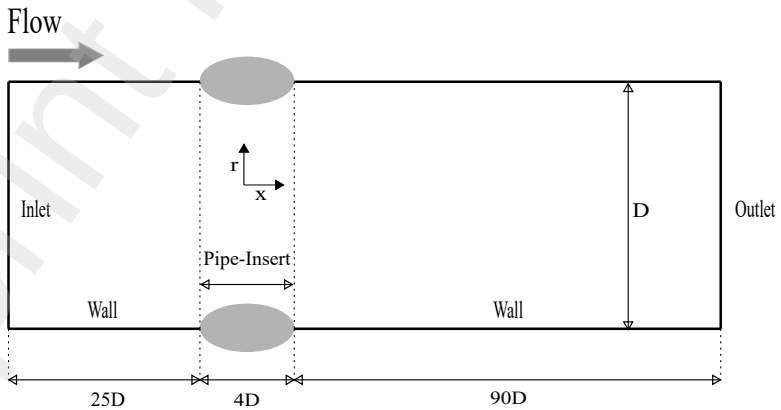

Figure 4: Computational domain employed for the current study (not to scale).

putational domain was tested by performing a domain sensitivity analysis, details of which are presented in Section 3. Schematics of the computational domain is illustrated in Fig. 4, which consisted of an insertion section ($4D$) that was preceded and tailed by upstream ($25D$) and downstream ($90D$) smooth sections. These upstream and downstream sections were implemented for smooth transition and recovery of the fully-developed turbulent flow, respectively. This domain configuration was utilized previously by Goswami and Hemmati [53, 54] and Masoumifar et al. [42, 43].

A nonuniform structured grid, containing 12.6×10^6 hexahedral elements, was used for the simulations. In order to accurately simulate the critical flow region, the grid was refined close to the insert and expanded towards the domain boundaries. The grid expansion ratio was maintained below 1.02 to avoid high-skewed elements and enhance the grid quality. Fig. 5 shows the grid density over the pipe cross-sectional and axial planes. The non-dimensional wall-normal spacing of the first cell (r^+) was kept below 2.0. Details on grid-sensitivity study are discussed in Section 3.

An initial simulation using a smooth pipe was performed to generate a fully developed velocity distribution at $Re = 7.5 \times 10^4$ for the inlet of our main simulations. The axial length of the smooth pipe was $220D$, following the experiments of Van Buren et al. [41] and the simulations of Masoumifar et al. [42, 43]. The fully-developed velocity profile was then mapped and implemented as an inlet boundary condition for the main simulations at the same Reynolds number. Neumann boundary condition was set for the pressure field at the inlet boundary and for all variables at the outlet boundary. The pipe wall was subjected to a no-slip boundary condition, $u_i = 0$. Thermally, a uniform temperature profile was set at the inlet boundary and a isoflux boundary condition was applied at the wall.

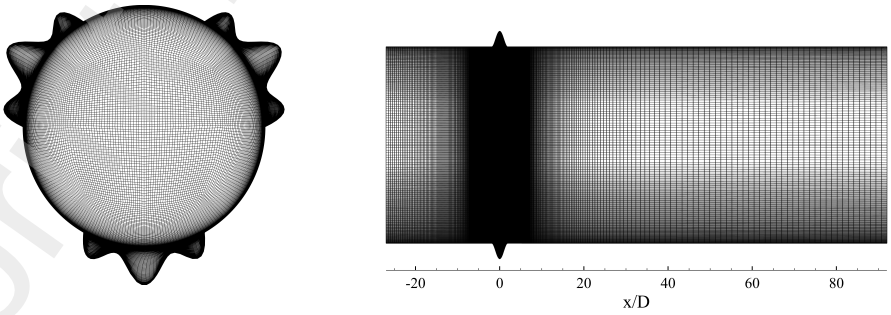

Figure 5: Grid density over the pipe cross-sectional and axial planes. Case III is depicted.

The governing equations were discretized based on finite-volume approach and solved using BuoyantSimpleFoam, which is a steady-state OpenFOAM solver for heat transfer citegreenshields2015openfoam. Semi-Implicit Method for Pressure-Linked Equations (SIMPLE) algorithm was adopted for modeling the coupling between pressure and velocity fields. The advection and diffusion terms were both discretized using second-order accurate discretization schemes. The numerical simulations were deemed to be numerically converged when the root-mean-square of momentum and energy residuals dropped below 10^{-6}. The simulations were performed using Compute Canada Clusters, utilizing 48 CPUs in parallel and memory of 190 GB.

3. Verification and validation studies

3.1. Domain sensitivity study

The adequacy of our computational domain to properly capture the main flow features in the critical region was verified using three different domain sizes with total axial lengths of $109D$ (Domain 1), $119D$ (Domain 2), and $129D$ (Domain 3). This was completed through successive extensions of the axial distance, downstream of the pipe-insert. The domain sensitivity analysis is only presented for the superimposed wall shape targeting the azimuthal Fourier mode of $m = 3 + 15$ (Case III) at $Re = 7.5 \times 10^4$. However, we further assured the suitability of domain size for Case I and Case II. Fig. 6 depicts variations of mean streamwise velocity and turbulent kinetic energy along the wake centerline, downstream of the pipe-insert. The results revealed that Domain 2 and Domain 3 had sufficient sizes to correctly capture the flow recovery. A maximum difference of less than 2% was obtained from results of Domain 2 and Domain 3, which

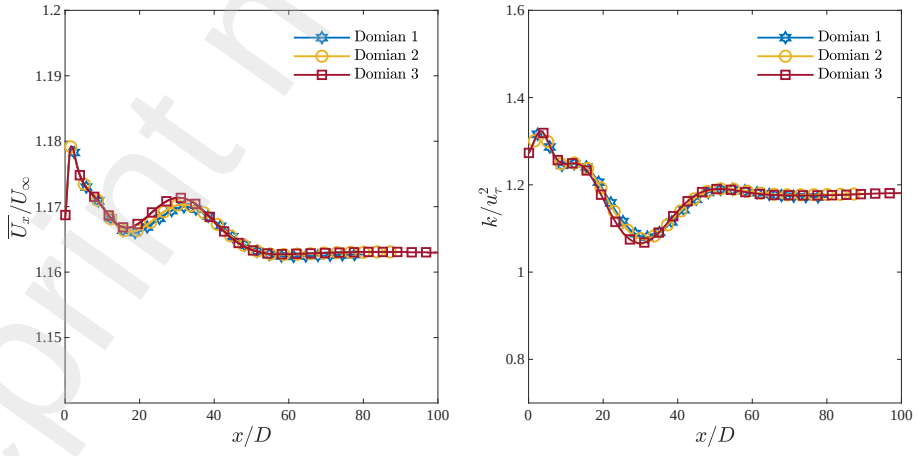

(a) (b)

Figure 6: Impact of domain size on (a) mean streamwise velocity and (b) turbulent kinetic energy.

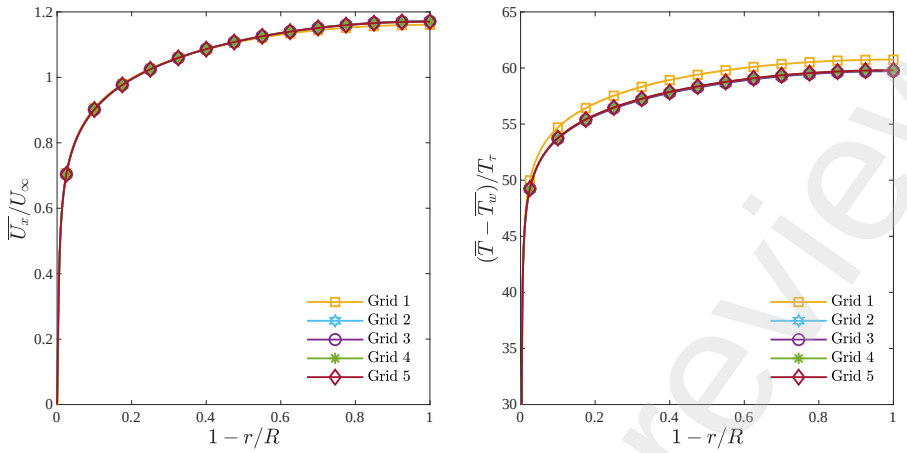

(a) (b)

Figure 7: Impact of grid refinement on (a) mean streamwise velocity and (b) mean temperature, at $x/D = 30$.

confirmed the minor effects of the outlet boundary condition on numerical predictions immediately after the perturbation. Thus, Domain 2 was utilized in the present investigation.

3.2. Grid sensitivity study

In an attempt to establish grid-independent results and to examine the quality of our grid, the results from five different grids were quantitatively analyzed based on Case III at $Re = 7.5 \times 10^4$. These five grids were designed by successively increasing grid resolution in the radial, circumferential, and axial directions. Table 2 outlines the specifics of each grid design. The grid sensitivity analysis was completed by studying impacts of the grid on radial distributions of time-averaged streamwise velocity and temperature at different axial locations. For brevity, the radial comparisons of quantities of interest are only presented and discussed at $x/D = 30$. Variations of the mean axial velocity

Table 2: Grid specifications based on Case III. $\Delta\theta^+$ and Δx^+ are the non-dimensional spacing in the azimuthal and streamwise directions in wall units, respectively. L_{pipe} is the axial pipe length and N_{total} represents the total number of hexahedral elements.

Study	L_{pipe}	N_{total}	r^+	$\Delta\theta^+$	Δx^+
Domain 1	$109D$	12.2×10^6	2	48	49
Domain 2	$119D$	12.6×10^6	2	48	49
Domain 3	$129D$	13.0×10^6	2	48	49
Grid 1	$119D$	8.8×10^6	4	55	49
Grid 2	$119D$	9.3×10^6	2	48	82
Grid 3	$119D$	10.7×10^6	2	48	64
Grid 4	$119D$	12.6×10^6	2	48	49
Grid 5	$119D$	14.2×10^6	2	48	40

and temperature profiles exhibited a small difference (< 2%) between Grid 4 and Grid 5, as demonstrated in Fig. 7. Therefore, the less computationally demanding grid size (Grid 4) was selected for the current study.

3.3. Validation of turbulence model

Validation studies were conducted to examine the accuracy of the simulations to predict the mean flow and thermal features of a turbulent pipe flow. This was performed by simulating a steady-state turbulent flow with heat transfer in a smooth pipe at $Re = 7.5 \times 10^4$ using $k - \omega$ (SST) turbulence model. Through a radial comparison of mean streamwise velocity profile against available experimental data, it was demonstrated that numerical results accord well with the experiment of Mckeon et al. [55], as shown in Fig. 8. More specifically, the maximum deviation was within 5% compared to the experimental data. Further, the numerically calculated fully developed Nusselt number was compared with Petukhov correlation to evaluate heat transfer modeling. We found that the numerical prediction of Nusselt number was in good agreement with Petukhov correlation [56], corresponding to a deviation of less than 8.0%. This confirmed the sufficient accuracy of the utilized numerical model in estimating the main flow and heat transfer characteristics of turbulent smooth pipeflow.

Table 3: Comparing Nusselt number from simulation with Petukhov correlation.

Study	*Nu*	Deviation
Petukhov correlation [56]	434.5	
Current study	400.7	7.8%

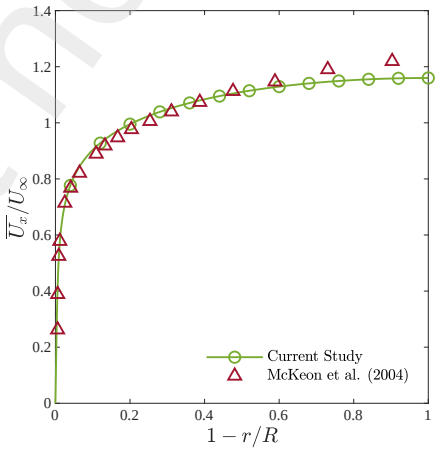

Figure 8: Comparing the numerical results of mean streamwise velocity with available experimental data.

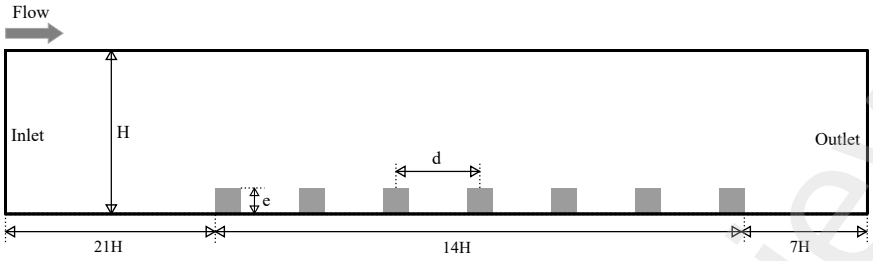

Figure 9: Schematics of the numerical setup with multiple square ribs employed for validation (not to scale).

It is important to indicate that there are no experiments and DNS simulations in literature, which include a detailed analysis of hydrodynamic and thermal characteristics in the presence of targeted pipe perturbations. This has restrained our ability to validate the model predictions of the targeted cases (m = 3 Case I, m = 15 Case II, m = 3 + 15 Case III) with experimental or DNS results. However, the validation study was extended by performing a simulation on turbulent channel flow with heat transfer perturbed by multiple square ribs. This was conducted to thoroughly evaluate the capability of our model in estimating mean flow and thermal features in the existence of geometrical modifications.

Fig. 9 presents schematics of the numerical setup, which was constructed based on the experiment of Tanda [57]. Here, the domain includes a ribbed segment ($x = 14H$) with a total of seven square ribs, placed periodically on the lower wall. The rib dimension was $e/H = 0.15$ and the pitch length was set as $d/H = 2.0$. A non-homogeneous mesh was employed for this validation study with a total of 5.6×10^5 elements. The r^+ of less than 4.0 was utilized and the maximum expansion ratio was kept below 1.02. The governing equations were solved in a $2D$-plane at $Re = 2.85 \times 10^4$. Uniform velocity and temperature distributions were set at the inlet. A Neumann boundary condition was specified for the pressure field at the inlet and for all flow and thermal properties at the outlet boundary. An isoflux boundary condition was subjected on the lower channel wall, and the upper wall and rib surfaces were deemed insulated, based on the experimental setup of Tanda [57].

Table 4: Friction factor (f) of turbulent channel flow with square roughness elements at $Re = 2.85 \times 10^4$.

Study	f	Deviation
Tanda [57]	0.0301	
Present study	0.0281	6.6%

The friction factor was numerically calculated and compared with the experiment of Tanda [57] in Table 4. The comparison returned a difference of 6.6% in the prediction of f value. To examine the accuracy of numerical predictions to heat transfer features, we validated the distribution of local Nusselt number within the ribbed segment against the experiment of Tanda [57] in Fig. 10. We found that our model generated compara-

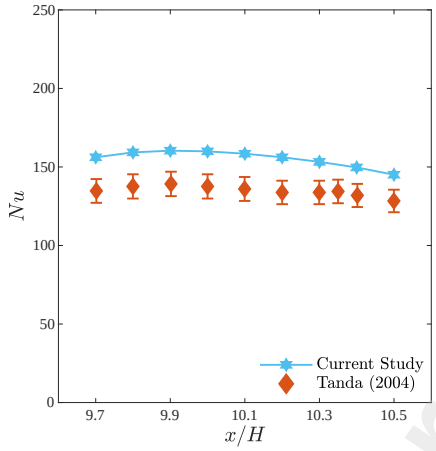

Figure 10: Variations of local Nusselt number of turbulent channel flow obstructed by square ribs. Error bars are depicted based on the experimental study of Tanda [57]

ble results to the experimental data. The maximum difference was less than 16% compared to the experiment. The deviations in the numerical predictions of friction factor and Nusselt number were within the acceptable range, noting that the uncertainty analysis in experimental values of f and Nu were $\pm 3.4\%$ and $\pm 5.6\%$, respectively, [57]. Thus, the extensive validation studies conducted here have proved the adequacy of our numerical model, in particular the SST $k-\omega$ turbulence model, in predicting mean hydrodynamic and thermal characteristics. This finding was also consistent with former investigations [47, 48, 52, 50] that evaluated the accuracy of numerical simulations and SST $k-\omega$ turbulence model in predicting thermofluid features.

4. Results and discussion

We begin by examining effects of the adopted wall modifications on radial profiles of mean axial velocity through comparisons against fully-developed state in Figs. 11(a-c). The fully-developed condition corresponds to the flow and thermal state at $x/D = 90$, downstream of the insertion section, where no variations in the flow and thermal characteristics were detected in comparison to fully-developed smooth pipe flow at similar operating conditions. The mean streamwise (axial) velocity ($\overline{U_x}$) was normalized using inlet bulk velocity (U_∞) and the radial coordinate (r/R) was normalized by the pipe radius. Variations in streamwise velocity profiles were defined by evaluating local differences (Δ) from fully developed state at $x/D = 90$. Particularly, the radial variations of mean axial velocity were examined at selected axial positions within $2D - 40D$, downstream of the pipe-insert section. Due to the modifications in wall geometry within the pipe-insert segment, the mean axial flow exhibited a velocity-deficit characteristic in near-wall region ($0 < r/R < 0.2$), immediately downstream of the

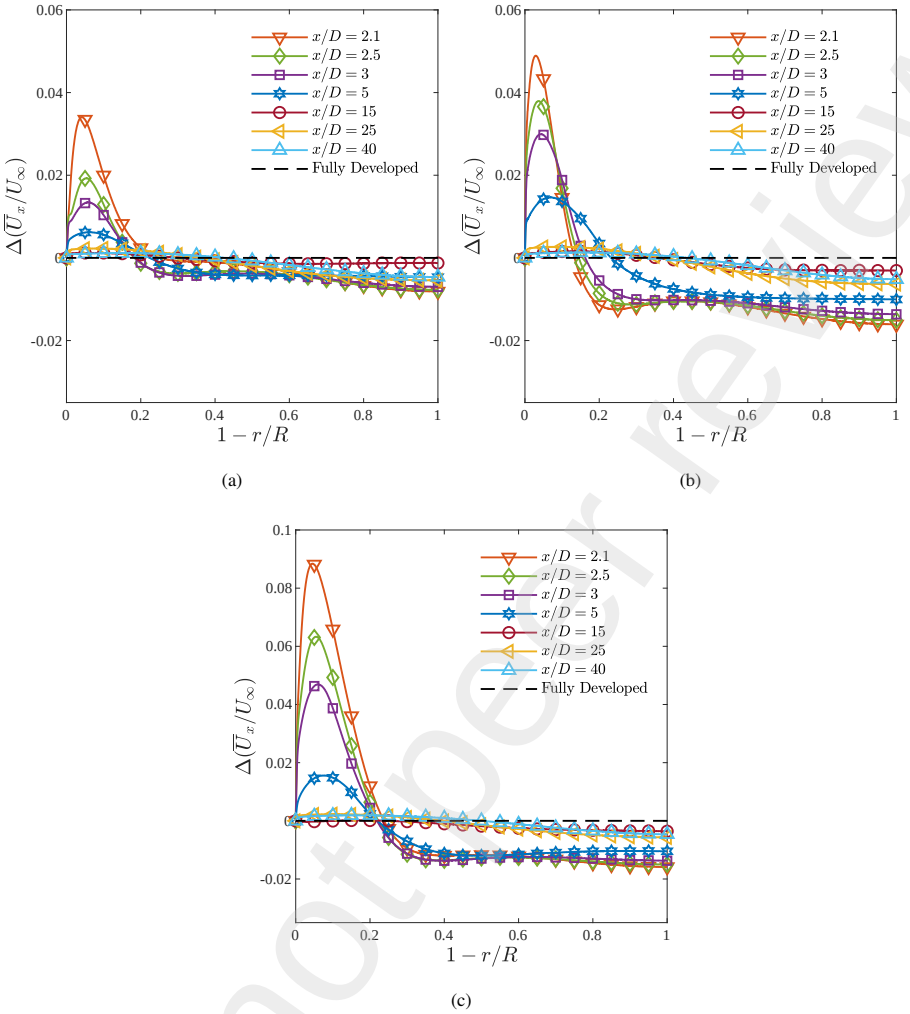

Figure 11: Evolution of mean axial velocity profiles for (a) Case I, (b) Case II, (c) Case III.

pipe insert, for all three cases. The deficit in velocity fields is presented in Figs. 11(a-c) as overshoots above the fully-developed state for all three wall shapes. The velocity deficit was balanced by an increase in magnitude of velocity at the outer region. This was consistent with the observations of Van Buren et al. [41] and Masoumifar et al. [42, 43], which elaborated that these wall modifications caused a deceleration and acceleration of mean flow in the near-wall and core flow regions, respectively. The flow adjustments in the core region to balance the velocity deficit in the near-wall region were ascribed to the nature of wall-bounded flows (e.g., channel and pipe flows) [58]. The cross-sectional contours of Fig. 12 clearly indicate that the deficit in velocity distribution close to the pipe wall was higher in magnitude for Case II and Case III, compared to the lower Fourier mode wall shape (Case I). This observation remained

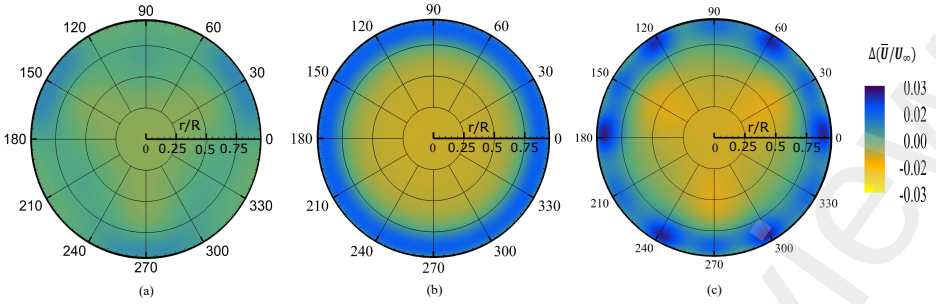

Figure 12: Cross-sectional contours of mean axial velocity at $x/D = 5$ for (a) Case I, (b) Case II, and (c) Case III).

intact downstream of the pipe-insert until the flow recovered to the fully-developed condition. On the thermal and heat flow, the flow deceleration in the near-wall region hinted at a decrease in magnitude of local convective heat transfer in the downstream region. Therefore, the targeted changes in wall shape could cause a drop in local Nusselt number (Nu) distribution after the pipe insert, leading to mitigation of heat loss to surroundings (e.g., ground formations in geothermal applications).

We further examined the axial velocity variations along the wake centerline for all three cases in Fig. 13. Here, the maximum velocity magnitude from fully-developed profile is used to normalize the axial velocity variations. Fig. 13 depicts a non monotonic (oscillatory) flow response for all three cases, such that a peak appears to exist at $x/D = 32$. Past this peak, the flow was noticed to recover towards the fully-developed flow condition for all wall shapes. A similar flow behaviour in the mean velocity profile has been formerly depicted in previous studies of non-equilibrium turbulent flows [59].

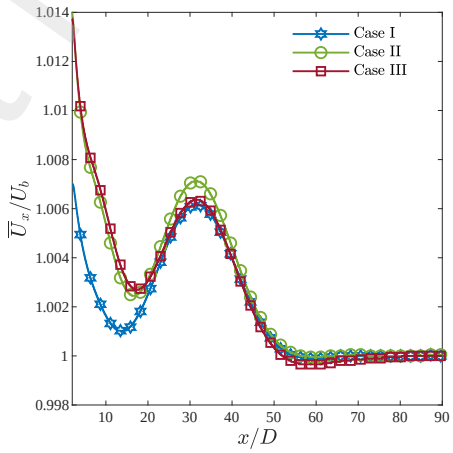

Figure 13: Variations of streamwise velocity along the wake centerline for all wall shapes.

The recovery process of $\overline{U_x}/U_\infty$ was investigated for all three cases in the downstream region by depicting the flow relaxation to the fully-developed condition. The recovery behaviour was examined based on maximum variations of less than 0.5% compared to fully-developed condition. We noticed that all three cases showed a delay in retrieving a recovered condition until $x \approx 40D$. This delayed recovery was attributed to the presence of the non-monotonic and oscillating flow response in the downstream region.

The distribution of time-averaged skin friction coefficient along the axial direction is illustrated in Fig. 14a. The skin friction coefficient was calculated by integrating over the circumferential direction of the pipe wall based on $C_f = \tau_w/0.5\rho U_\infty^2$, where τ_w is the wall shear stress. Skin-friction coefficient (C_f) was normalized by its far downstream value ($C_{f,b}$) at $x/D = 90$, where there exist no variations in flow and thermal characteristics compared to fully-developed smooth-pipe conditions. The axial location was normalized by the pipe diameter D. The distribution of skin friction coefficient exhibited a substantial decrease in magnitude for all cases, compared to the smooth pipe flow at similar operating conditions, before relaxing towards the fully-developed condition. The maximum percentage reductions of C_f were 12.5%, 17.4%, and 16.5% for Case I, Case II, and Case III, respectively (see Fig. 14b). The decrease in skin friction coefficient was attributed to the flow deceleration and reduced velocity gradients in proximity of the pipe wall. This observation agrees well with previous studies, which confirm the capacity of generating reduced-momentum flow close to the wall as a successful flow mechanism to reduce frictional drag [60, 61, 62, 63, 33]. Downstream the pipe-insert within $x = 2D - 10D$, the average reductions in frictional drag were 1.6%, 5.0%, and 4.7% for Case I, Case II, and Case III, respectively. The higher frictional

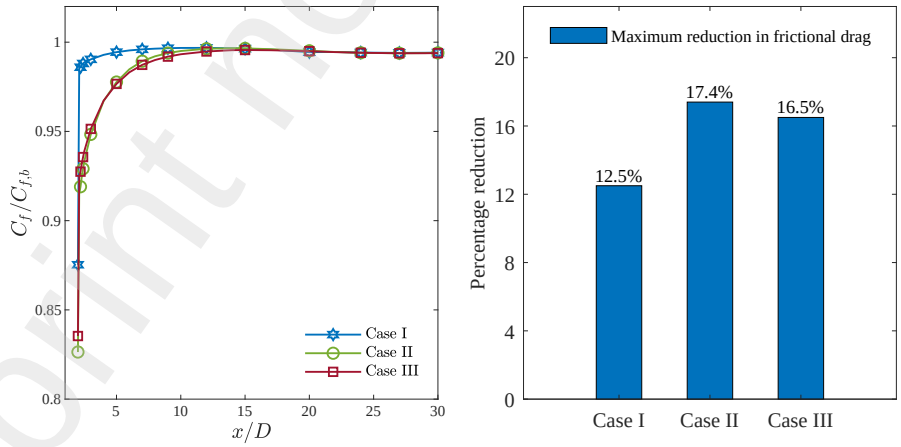

Figure 14: Impacts of targeted pipe-inserts on frictional drag, (a) variations of C_f along the wake axial direction, and (b) maximum frictional-drag reductions for all cases.

drag reductions of Case II and Case III were linked to the greater capability of those shapes in decelerating the flow close to the wall compared to Case I. Hence, we can confirm that the targeted wall modifications were capable of generating a downstream zone of reduced drag and lower surface friction. From a practical perspective, these reductions in skin-friction drag translate into economical and environmental benefits pertinent to several engineering applications (e.g., extraction processes in geothermal systems).

The modified thermal response to the targeted wall shapes is evaluated through inspecting variations in radial profiles of mean temperature with respect to the fully-developed state in Fig. 15. The mean temperature was normalized by friction temperature, based on $T_\tau = q_w/\rho C_p u_\tau$, where q_w is the uniform heat flux imposed on

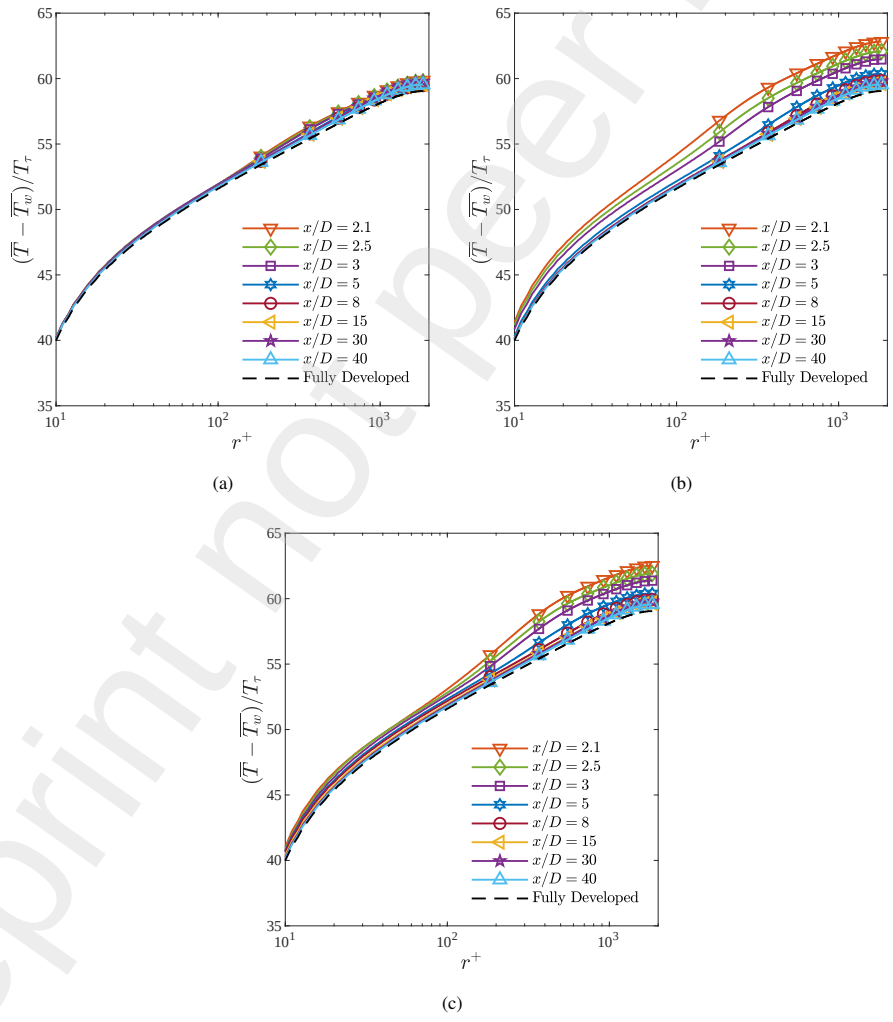

Figure 15: Mean temperature profile development for (a) Case I, (b) Case II, (c) Case III.

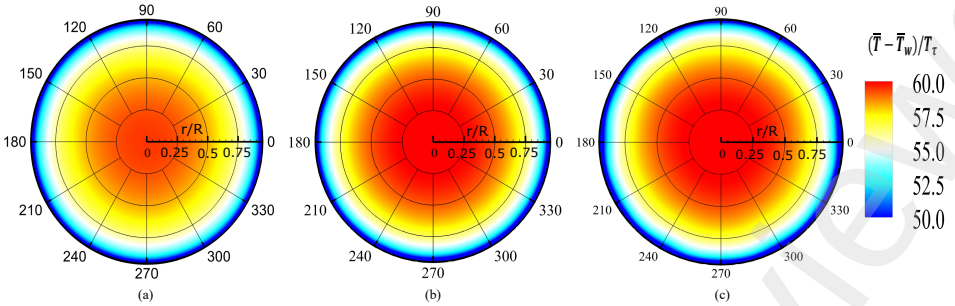

Figure 16: Contours of mean temperature at $x/D = 5$ for (a) Case I, (b) Case II, and (c) Case III).

the pipe wall and u_τ is friction velocity. Immediately downstream of the pipe-insert at $x/D = 2.1$, all three cases showed an increase in magnitude of the mean temperature along the radial direction ($r^+ > 10$) compared to the fully-developed state. This was followed by a relaxation of the mean temperature, within $2D - 40D$, towards the fully-recovered condition. The presented results confirmed that the targeted wall perturbations caused an attenuation in strength of the convective heat transfer mechanism, which resulted in higher fluid temperature, downstream of the pipe insert. This was attributed to the decelerated flows and reduced velocity gradients in the near-wall region, as depicted previously in Fig. 11. This interpretation was consistent with the discussions of Ramgadia and Saha [33], while investigating the variations of turbulent heat transfer characteristics in downhill surface of wavy-wall duct. More recently, Castellanos et al. [64] linked the attenuation in convective heat transfer to the deliberate formation of momentum deficit within the boundary layer. We further looked at the recovery of mean dimensionless temperature by tracing their relaxation behavior towards the fully-developed state within $2D - 40D$, downstream of the pipe perturbation. All three cases depicted a prolong recovery trend, such that the fully-recovered thermal state was attained within $x \approx 40D$. The similarities in the recovery behavior between mean axial velocity and temperature implied that the heat transfer recovery was mainly dominated by velocity gradients downstream of the pipe-insert. The contour plots of mean temperature in Fig. 16 reveal that the pipe perturbations of Case II and Case III depicted higher impact in mitigating convective heat transfer in the near-wall region compared to Case I, thereby leading to the fluid possessing increased temperature at the core. This was attributed to the stronger effect of Case II and Case III in reducing flow momentum close to the pipe wall.

To quantitatively assess the influence of targeted wall shapes on convective heat transfer, the cross-sectional-averaged Nusselt number was computed at several axial locations downstream of the pipe insert (Fig. 17a). Local Nusselt number (Nu) was calculated based on $Nu = hD/k_f$, where h is the convective heat transfer coefficient.

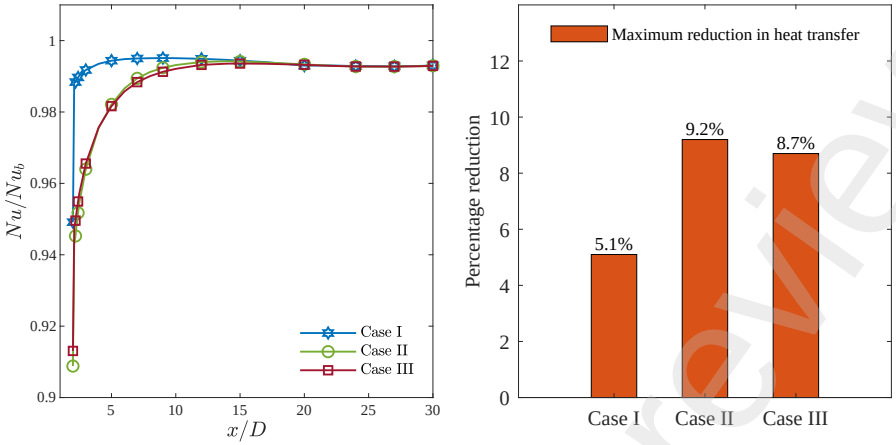

Figure 17: Effects of targeted pipe-inserts on convective heat transfer. (a) variations of Nu along the wake axial direction, and (b) maximum heat transfer reductions for all cases.

Nusselt number (Nu) was normalized by its far downstream value (Nu_b) at $x/D = 90$. The axial variations of local Nusselt number indicated an initial drop in magnitude for all wall shapes, before approaching the fully recovered state. The results demonstrated a maximum reduction of 5.1% in near-wall convective heat transfer with the lower Fourier mode ($m = 3$) wall modification (see Fig. 17b). In contrast, Case II and Case III generated greater inhibition to convective heat transfer with a maximum reduction of ~9% in Nusselt number at the onset of the downstream section. This indicates to the capability of the targeted wall perturbations in reducing convective heat transfer, hence presenting feasibility to inhibit heat losses to ground rock formations in geothermal systems. Within a downstream region of $x = 2D - 10D$, the average inhibitions in near-wall convective heat transfer were 1.1%, 3.4%, and 3.2% for Case I, Case II, and Case III, respectively. It is essential to indicate that we conducted a separate study to assess implications of pipe insert targeting the higher Fourier mode ($m = 15$) at a range of Reynolds numbers [65], corresponding to different subsurface thermal systems, i.e., geothermal wellsites. The results in Fig. 18 confirmed the capability of the targeted wall perturbation in reducing frictional drag and convective heat transfer for all examined Reynolds numbers, hence presenting feasibility to inhibit energy losses in geothermal processes. These effects were magnified at lower Reynolds numbers, which is more closely linked to conventional subsurface thermal energy systems. Through a close inspection of Fig. 17b, we noticed a self-similar thermal response and recovery for Case II and Case III. This self-similarity indicated to a predominant impact of the higher Fourier mode ($m = 15$) wall shape on manipulating the heat transfer characteristics and recovery. Further, a qualitative comparison between Figs. 14a and 17a re-

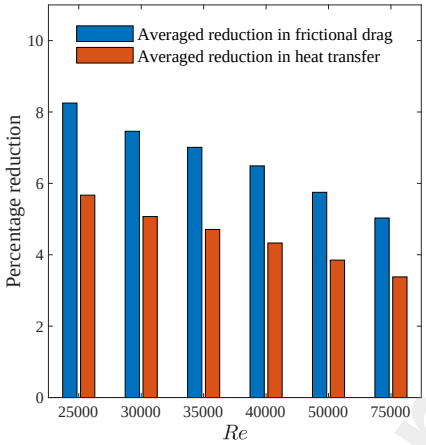

Figure 18: Averaged reductions in frictional drag and heat transfer within $x = 2D - 10D$ for Case II at a range of Reynolds numbers.

vealed that the distributions of Nu and C_f along the axial direction are well correlated. This was referred to the characteristic nature of forced-convection flows, which dictate the correlation between temperature and velocity gradients [33]. The results thus far clearly confirm the impacts of the targeted wall shapes on manipulating flow and thermal characteristics towards reducing convective heat transfer and frictional drag in the downstream zone, thus presenting capability to minimize heat losses to ground formations pertinent to geothermal applications with saving pumping power.

5. Conclusion

The current study numerically examined the hydrodynamic and thermal characteristics of a new flow manipulation technique for subsurface casings in, for example, geothermal facilities. Particularly, we investigated flow and convective heat transfer features of turbulent pipe flow experiencing sudden variations in wall geometry at Reynolds number of 7.5×10^4. The modified wall conditions were designed to best replicate particular azimuthal Fourier modes corresponding to $m = 3$, $m = 15$, and $m = 3 + 15$, which were placed in the middle of a smooth pipe. The final design would incorporate intermittent placement of pipe-inserts in subsurface casings at fixed intervals. The targeted wall perturbations generated long-lasting variations in flow and convective heat transfer properties in favor of mitigating heat losses to subsurface rock formations in geothermal systems, while lowering pumping power requirement. This provided a potential approach towards increasing the efficiency of geothermal systems. In response to the wall modifications, mean axial flow exhibited deceleration and reduced velocity gradients in near-wall region for all three cases. These modified flow characteristics contributed to local reduction in convective heat transfer, thus presenting

the capability to suppress heat losses in geothermal applications. Particularly, the wall modifications of $m = 15$ and $m = 3 + 15$ resulted in a maximum decrease of ~9% in convective heat transfer coefficient, immediately after the pipe-insert section compared to smooth-pipe flow at similar working conditions. This was escorted by reductions in frictional drag, which quantified as ~17.4% and ~16.5% for wall modifications of $m = 15$ and $m = 3 + 15$, respectively. Within a downstream zone of $2D - 10D$, the averaged reductions in heat transfer and frictional drag for the wall shape of $m = 15$ corresponded to 3.4% and 5.0%, respectively. The mean temperature profiles revealed a similar thermal response of the higher and combined Fourier modes ($m = 15$ and $m = 3 + 15$), such that the fully-developed thermal state was depicted at $x = 40D$ from the perturbation. The perturbed wall condition of $m = 3$ led to averaged reductions of ~1.1% and ~1.6% in near-wall convective heat transfer and frictional drag within $2D - 10D$, respectively.

CRediT authorship statement

Nawaf Salem: Conceptualization, Methodology, Software, Data Curation, Investigation, Validation, Formal analysis, Visualization, Writing - Original Draft. **Ali Tarokh:** Conceptualization, Supervision, Writing - Review & Editing, Project administration. **Arman Hemmati:** Conceptualization, Resources, Supervision, Writing - Review & Editing, Funding acquisition, Project administration.

Declaration of competing interest

The authors declare that they have no known competing financial interests or personal relationships that could have appeared to influence the work reported in this paper.

Data availability statement

The data that demonstrate the outcomes of this investigation are available within the article.

Acknowledgment

The present study has received support from Alberta Innovate, National Science and Engineering Research Council of Canada (NSERC) Alliance, and Imperial Oil. Compute Canada clusters were operated to run the required simulations.

References

[1] T. B. Johansson, J. Goldemberg, Energy for sustainable development: a policy agenda.

[2] J. L. Sawin, F. Sverrisson, K. Seyboth, R. Adib, H. E. Murdock, C. Lins, I. Edwards, M. Hullin, L. H. Nguyen, S. S. Prillianto, et al., Renewables 2017 global status report.

[3] C. Wolf, D. Klein, K. Richter, G. Weber-Blaschke, Environmental effects of shifts in a regional heating mix through variations in the utilization of solid biofuels, Journal of Environmental Management 177 (2016) 177–191.

[4] X. Hu, J. Banks, Y. Guo, W. V. Liu, Utilizing geothermal energy from enhanced geothermal systems as a heat source for oil sands separation: A numerical evaluation, Energy 238 (2022) 121676.

[5] M. Günther, T. Hellmann, International environmental agreements for local and global pollution, Journal of Environmental Economics and Management 81 (2017) 38–58.

[6] M. Soltani, F. M. Kashkooli, A. Dehghani-Sanij, A. Kazemi, N. Bordbar, M. Farshchi, M. Elmi, K. Gharali, M. B. Dusseault, A comprehensive study of geothermal heating and cooling systems, Sustainable Cities and Society 44 (2019) 793–818.

[7] H. Garrett-Peltier, Green versus brown: Comparing the employment impacts of energy efficiency, renewable energy, and fossil fuels using an input-output model, Economic Modelling 61 (2017) 439–447.

[8] S. WEC, Survey of energy resources 2007, World Energy Council.

[9] R. Bertani, Geothermal power generation in the world 2005–2010 update report, geothermics 41 (2012) 1–29.

[10] R. DiPippo, J. L. Renner, Geothermal energy, in: Future Energy, Elsevier, 2014, pp. 471–492.

[11] R. Xu, L. Zhang, F. Zhang, P. Jiang, A review on heat transfer and energy conversion in the enhanced geothermal systems with water/co2 as working fluid, International Journal of Energy Research 39 (13) (2015) 1722–1741.

[12] J. W. Tester, B. J. Anderson, A. Batchelor, D. Blackwell, R. DiPippo, E. Drake, J. Garnish, B. Livesay, M. Moore, K. Nichols, et al., The future of geothermal energy, Massachusetts Institute of Technology 358.

[13] W. Kumari, P. Ranjith, Sustainable development of enhanced geothermal systems based on geotechnical research–a review, Earth-Science Reviews 199 (2019) 102955.

[14] T. X. Phuoc, M. Massoudi, P. Wang, M. L. McKoy, Heat losses associated with the upward flow of air, water, co2 in geothermal production wells, International Journal of Heat and Mass Transfer 132 (2019) 249–258.

[15] J. Wang, Energy recovery from oil sands reservoirs.

[16] S. Liu, M. Sakr, A comprehensive review on passive heat transfer enhancements in pipe exchangers, Renewable and sustainable energy reviews 19 (2013) 64–81.

[17] B. Lu, P.-X. Jiang, Experimental and numerical investigation of convection heat transfer in a rectangular channel with angled ribs, Experimental Thermal and Fluid Science 30 (6) (2006) 513–521.

[18] J.-A. Zambaux, J.-L. Harion, S. Russeil, P. Bouvier, The effect of successive alternating wall deformation on the performance of an annular heat exchanger, Applied Thermal Engineering 90 (2015) 286–295.

[19] R. Tiruselvam, W. Chin, V. R. Raghavan, Double tube heat exchanger with novel enhancement: part ii—single phase convective heat transfer, Heat and Mass Transfer 48 (8) (2012) 1451–1462.

[20] V. Kongkaitpaiboon, P. Promthaisong, V. Chuwattanakul, K. Wongcharee, S. Eiamsa-ard, Effects of spiral start number and depth ratio of corrugated tube on flow and heat transfer characteristics in turbulent flow region, Journal of Mechanical Science and Technology 33 (8) (2019) 4005–4012.

[21] P. Promthaisong, W. Jedsadaratanachai, S. Eiamsa-Ard, 3d numerical study on the flow topology and heat transfer characteristics of turbulent forced convection in spirally corrugated tube, Numerical Heat Transfer, Part A: Applications 69 (6) (2016) 607–629.

[22] L. Yang, K. Du, Z. Zhang, Heat transfer and flow optimization of a novel sinusoidal minitube filled with non-newtonian sic/eg-water nanofluids, International Journal of Mechanical Sciences 168 (2020) 105310.

[23] T. Alam, M.-H. Kim, A comprehensive review on single phase heat transfer enhancement techniques in heat exchanger applications, Renewable and Sustainable Energy Reviews 81 (2018) 813–839.

[24] B. Prasad, J. Saini, Effect of artificial roughness on heat transfer and friction factor in a solar air heater, Solar energy 41 (6) (1988) 555–560.

[25] P. Promvonge, C. Thianpong, Thermal performance assessment of turbulent channel flows over different shaped ribs, International Communications in Heat and Mass Transfer 35 (10) (2008) 1327–1334.

[26] S. Singh, B. Singh, V. Hans, R. Gill, Cfd (computational fluid dynamics) investigation on nusselt number and friction factor of solar air heater duct roughened with non-uniform cross-section transverse rib, Energy 84 (2015) 509–517.

[27] J.-A. Meng, X.-G. Liang, Z.-J. Chen, Z.-X. Li, Experimental study on convective heat transfer in alternating elliptical axis tubes, Experimental Thermal and Fluid Science 29 (4) (2005) 457–465.

[28] B. Li, B. Feng, Y.-L. He, W.-Q. Tao, Experimental study on friction factor and numerical simulation on flow and heat transfer in an alternating elliptical axis tube, Applied Thermal Engineering 26 (17-18) (2006) 2336–2344.

[29] S. Patankar, C. Liu, E. Sparrow, Fully developed flow and heat transfer in ducts having streamwise-periodic variations of cross-sectional area.

[30] Z. Guo, D. Li, B. Wang, A novel concept for convective heat transfer enhancement, International Journal of Heat and Mass Transfer 41 (14) (1998) 2221–2225.

[31] J. Meng, Enhanced heat transfer technology of longitudinal vortices based on field-coordination principle and its application, Power Engineering and Engineering Thermophysics, Tsinghua University, Beijing.

[32] H. N. Khaboshan, H. R. Nazif, The effect of multi-longitudinal vortex generation on turbulent convective heat transfer within alternating elliptical axis tubes with various alternative angles, Case studies in thermal engineering 12 (2018) 237–247.

[33] A. G. Ramgadia, A. K. Saha, Three-dimensional numerical study of turbulent flow and heat transfer in a wavy-walled duct, International Journal of Heat and Mass Transfer 67 (2013) 98–117.

[34] L. Goldstein Jr, E. M. Sparrow, Heat/mass transfer characteristics for flow in a corrugated wall channel.

[35] G. Wang, S. Vanka, Convective heat transfer in periodic wavy passages, International Journal of Heat and Mass Transfer 38 (17) (1995) 3219–3230.

[36] B. Ničeno, E. Nobile, Numerical analysis of fluid flow and heat transfer in periodic wavy channels, International Journal of Heat and Fluid Flow 22 (2) (2001) 156–167.

[37] H. S. Choi, K. Suzuki, Large eddy simulation of turbulent flow and heat transfer in a channel with one wavy wall, International journal of heat and fluid flow 26 (5) (2005) 681–694.

[38] N. Kruse, A. GÜnther, P. R. Von Rohr, Dynamics of large-scale structures in turbulent flow over a wavy wall, Journal of Fluid Mechanics 485 (2003) 87–96.

[39] N. Kruse, P. R. Von Rohr, Structure of turbulent heat flux in a flow over a heated wavy wall, International journal of heat and mass transfer 49 (19-20) (2006) 3514–3529.

[40] S. Kuhn, S. Kenjereš, P. R. von Rohr, Large eddy simulations of wall heat transfer and coherent structures in mixed convection over a wavy wall, International journal of thermal sciences 49 (7) (2010) 1209–1226.

[41] T. Van Buren, L. H. Hellstrom, I. Marusic, A. J. Smits, Turbulent pipe flow response to wall changes targeting specific azimuthal modes, in: Tenth International Symposium on Turbulence and Shear Flow Phenomena, Begel House Inc., 2017.

[42] M. Masoumifar, S. Verma, A. Hemmati, Effects of targeted wall geometries on response of turbulent pipe flow at high reynolds number, International Journal of Heat and Fluid Flow 92 (2021) 108882.

[43] M. Masoumifar, S. Verma, A. Hemmati, Response of turbulent pipe flow to targeted wall shapes at a range of reynolds numbers, Physics of Fluids 33 (6) (2021)

065105.

[44] J. H. Ferziger, M. Perić, R. L. Street, Computational methods for fluid dynamics, Vol. 3, Springer, 2002.

[45] S. W. Churchill, A reinterpretation of the turbulent prandtl number, Industrial & engineering chemistry research 41 (25) (2002) 6393–6401.

[46] F. Menter, T. Esch, Elements of industrial heat transfer predictions, in: 16th Brazilian Congress of Mechanical Engineering (COBEM), Vol. 109, 2001, p. 650.

[47] A. Chaube, P. Sahoo, S. Solanki, Analysis of heat transfer augmentation and flow characteristics due to rib roughness over absorber plate of a solar air heater, Renewable Energy 31 (3) (2006) 317–331.

[48] S. Eiamsa-ard, W. Changcharoen, Analysis of turbulent heat transfer and fluid flow in channels with various ribbed internal surfaces, Journal of Thermal Science 20 (3) (2011) 260–267.

[49] N. Zheng, W. Liu, Z. Liu, P. Liu, F. Shan, A numerical study on heat transfer enhancement and the flow structure in a heat exchanger tube with discrete double inclined ribs, Applied Thermal Engineering 90 (2015) 232–241.

[50] N. Zheng, P. Liu, F. Shan, Z. Liu, W. Liu, Heat transfer enhancement in a novel internally grooved tube by generating longitudinal swirl flows with multi-vortexes, Applied Thermal Engineering 95 (2016) 421–432.

[51] N. Zheng, P. Liu, F. Shan, Z. Liu, W. Liu, Turbulent flow and heat transfer enhancement in a heat exchanger tube fitted with novel discrete inclined grooves, International Journal of Thermal Sciences 111 (2017) 289–300.

[52] X. Tang, X. Dai, D. Zhu, Experimental and numerical investigation of convective heat transfer and fluid flow in twisted spiral tube, International Journal of Heat and Mass Transfer 90 (2015) 523–541.

[53] S. Goswami, A. Hemmati, Response of turbulent pipeflow to multiple square bar roughness elements at high reynolds number, Physics of Fluids 32 (7) (2020) 075110.

[54] S. Goswami, A. Hemmati, Evolution of turbulent pipe flow recovery over a square bar roughness element at a range of reynolds numbers, Physics of Fluids 33 (3) (2021) 035113.

[55] B. J. Mckeon, J.-d. Li, W. Jiang, J. F. Morrison, A. J. Smits, Further observations on the mean velocity distribution in fully developed pipe flow, Journal of Fluid Mechanics 501 (2004) 135–147.

[56] B. Petukhov, Heat transfer and friction in turbulent pipe flow with variable physical properties, in: Advances in heat transfer, Vol. 6, Elsevier, 1970, pp. 503–564.

[57] G. Tanda, Heat transfer in rectangular channels with transverse and v-shaped broken ribs, International Journal of Heat and Mass Transfer 47 (2) (2004) 229–243.

[58] T. Van Buren, D. Floryan, L. Ding, L. Hellström, A. Smits, Turbulent pipe flow response to a step change in surface roughness, Journal of Fluid Mechanics 904.

[59] A. J. Smits, S. Young, P. Bradshaw, The effect of short regions of high surface curvature on turbulent boundary layers, Journal of fluid mechanics 94 (2) (1979) 209–242.

[60] W. Schoppa, F. Hussain, A large-scale control strategy for drag reduction in turbulent boundary layers, Physics of Fluids 10 (5) (1998) 1049–1051.

[61] X. Cheng, C. Wong, F. Hussain, W. Schröder, Y. Zhou, Flat plate drag reduction using plasma-generated streamwise vortices, Journal of Fluid Mechanics 918.

[62] R. D. Whalley, K.-S. Choi, Turbulent boundary-layer control with plasma spanwise travelling waves, Experiments in Fluids 55 (8) (2014) 1–16.

[63] Y. Du, V. Symeonidis, G. Karniadakis, Drag reduction in wall-bounded turbulence via a transverse travelling wave, Journal of fluid mechanics 457 (2002) 1–34.

[64] R. Castellanos, T. Michelis, S. Discetti, A. Ianiro, M. Kotsonis, Reducing turbulent convective heat transfer with streamwise plasma vortex generators, Experimental Thermal and Fluid Science 134 (2022) 110596.

[65] N. Salem, A. Tarokh, A. Hemmati, Reynolds number effects on heat transfer and frictional drag implications of turbulent pipeflow past targeted wall shapes (under review), Physics of Fluids.